
PRECIPITATION DOWNSCALING WITH SPATIOTEMPORAL VIDEO DIFFUSION

Prakhar Srivastava^{*1}, Ruihan Yang^{†1}, Gavin Kerrigan^{‡1}, Gideon Dresdner^{§2}, Jeremy McGibbon^{¶2}, Christopher Bretherton^{||2}, and Stephan Mandt^{**1}

¹Department of Computer Science, University of California, Irvine

²Allen Institute for AI

ABSTRACT

In climate science and meteorology, high-resolution local precipitation (rain and snowfall) predictions are limited by the computational costs of simulation-based methods. Statistical downscaling, or super-resolution, is a common workaround where a low-resolution prediction is improved using statistical approaches. Unlike traditional computer vision tasks, weather and climate applications require capturing the accurate conditional distribution of high-resolution given low-resolution patterns to assure reliable ensemble averages and unbiased estimates of extreme events, such as heavy rain. This work extends recent video diffusion models to precipitation super-resolution, employing a deterministic downscaler followed by a temporally-conditioned diffusion model to capture noise characteristics and high-frequency patterns. We test our approach on FV3GFS output, an established large-scale global atmosphere model, and compare it against five state-of-the-art baselines. Our analysis, capturing CRPS, MSE, precipitation distributions, and qualitative aspects using California and the Himalayas as examples, establishes our method as a new standard for data-driven precipitation downscaling.

1 Introduction

Patterns of precipitation (rainfall and snowfall) are central to human and natural life on earth. In a rapidly warming climate, reliable simulations of how precipitation patterns may change can help human societies adapt to climate change. However, such simulations are challenging as weather systems vary over many scales in space and time. Moreover, interactions with complex surface features such as mountains and coastlines contribute to precipitation trends and extremes [48]. For many purposes, such as estimating flood hazards, precipitation must be estimated at a spatial resolutions of only a few kilometers. Fluid-dynamical models of the global atmosphere are prohibitively expensive to run at such fine scales [55], so the climate adaptation community relies on “downscaling”⁸ of coarse-grid simulations to a finer grid. Traditional downscaling methods are either “dynamical” (running a fine-grid fluid-dynamical model limited to the region of interest, which requires specialized knowledge and computational resources) or “statistical” (typically restricted to simple univariate methods) [57]. Advances in super-resolution methods developed by the computer vision community are poised to dramatically improve statistical downscaling.

Such work is a natural follow-up to recent advancements in deep-learning-based weather and climate prediction methodologies, which have ushered in a new era of data-driven forecasting. These approaches show remarkable performance gains, boasting improvements of orders of magnitude in runtime without sacrificing accuracy [37, 24].

*prakhs2@uci.edu

†ruihan.yang@uci.edu

‡kerrigag@uci.edu

§gideond@allenai.org

¶jeremym@allenai.org

||christopherb@allenai.org

**mandt@uci.edu

⁸This is the climate science terminology for super-resolution.

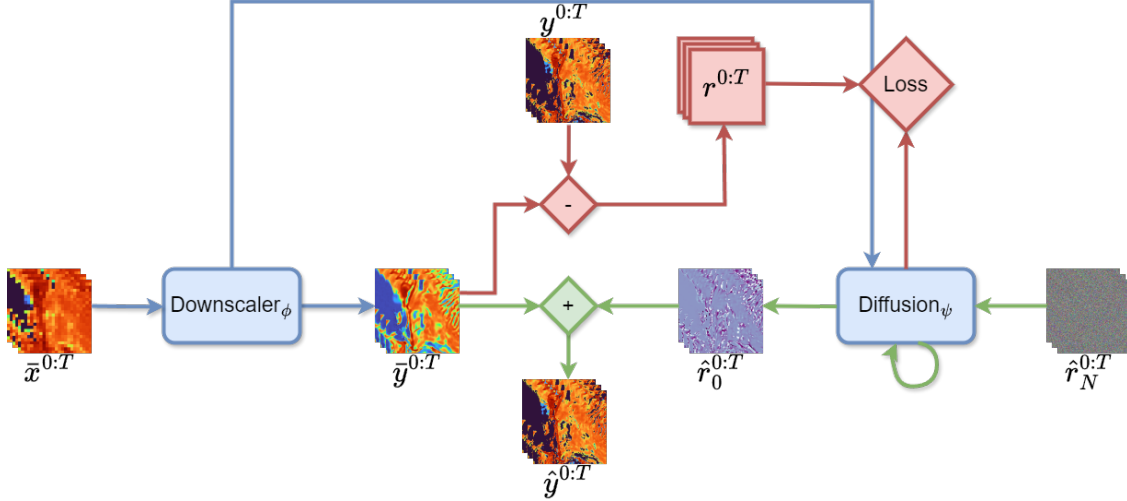


Figure 1: Illustration of our model’s training and inference pipelines. Blue blocks are common to both phases, red blocks are exclusive to training, and green blocks are for inference only. The model takes a low-resolution precipitation sequence, downscales it deterministically using spatio-temporal factorized attention, and models residual with conditional diffusion and factorized attention. Here, T denotes the sequence length, and N denotes the diffusion steps. The model parameters ($\theta = \phi, \psi$) are jointly optimized during training. See Appendix A.1 for further details on our model architecture.

Our focus centers on addressing a *temporal* downscaling problem. Our objective is to enhance the resolution of a sequence (“video”) of low-resolution precipitation frames into a sequence of high-resolution frames. Precipitation has strong temporal continuity on hourly time scales. Hence, despite the apparent differences between precipitation data and natural videos, we adopt ideas from video super-resolution to leverage information from multiple context frames to stochastically downscale the precipitation sequence [43, 33].

Until recently, endeavors to enhance the resolution of climate states like precipitation have been primarily based on deterministic regression methods that employ convolutions or transformers. However, super-resolution is a one-to-many mapping with a continuum of “correct” answers. Treating such one-to-many problems using supervised learning is therefore prone to visual artifacts since the supervised network tries to predict the average from a multitude of incompatible solutions. Such *mode averaging* is a known source of blurriness in visual data [25, 66]. Besides visual artifacts, mode averaging can have even more dramatic implications in climate and weather modeling, such as the underestimation of extreme precipitation, which is mainly induced by regional weather patterns on the unresolved scale. While some successful supervised super-resolution methods for images and video have been proposed [9, 22, 65, 8, 20], a natural approach to preventing mode averaging are conditional *generative models*, due to their ability to capture multi-modal conditional data distributions.

To that end, a line of recent work proposes the use of generative adversarial networks (GANs) for precipitation downscaling. These GAN-based methodologies often encounter challenges, displaying a tendency to converge on a specific mode of the data distribution, occasionally fixating on isolated points in extreme cases. Despite their perceptual appeal, the scientific utility of super-resolution necessitates the accurate modeling of the statistical *distribution* of high-resolution data given low-resolution input, a facet that GANs typically fall short of capturing.

In this paper, we propose Spatiotemporal Video Diffusion (STVD), a diffusion-based generative model for spatio-temporal precipitation downscaling. Our model uses a spatio-temporal factorized attention-based downscaler to incorporate temporal context, followed by modeling the residual error with a similar factorized attention-based conditional diffusion model, allowing us to add finer details to the coarse prediction made by the downscaler. Diffusion models are particularly well-suited for precipitation downscaling, as they have been shown to successfully capture high dimensional and multimodal distributions, alleviating a key drawback of GAN-based methods for climate science applications.

This study underscores the capability of conditional diffusion models to meet the specific needs of statistical precipitation downscaling. Specifically, our contributions are:

1. We introduce a novel framework for temporal precipitation downscaling using diffusion models. Our model combines a deterministic downscaling module with a diffusion-based residual module, leveraging spatiotemporal, factorized attention to process information from multiple low-resolution frames.
2. Our model outperforms five strong super-resolution baselines across multiple criteria, including MSE and several distributional metrics. We compare against two image super-resolution models and three video super-resolution models using the FV3GFS global atmosphere simulation dataset [67, 7].
3. Our approach captures key characteristics of precipitation, including extreme precipitation probabilities and spatial patterns of annual precipitation in mountainous regions, which are crucial for domain science applications.

Our paper is structured as follows. First, we describe our method (Sec. 2), which is then followed by a discussion on our experimental findings (Sec. 3). Lastly, we discuss relevant literature (Sec. 4) and its connection to our work.

2 Downscaling via Spatiotemporal Video Diffusion

2.0.1 Problem Statement

At training time, we assume that we have access to a collection of high-resolution precipitation frame sequences $\mathbf{y}^{0:T}$ and their corresponding low-resolution precipitation frame sequences $\mathbf{x}^{0:T}$. Such a low-resolution sequence can be obtained through area-weighted coarsening [34] of the corresponding high-resolution sequence. The dataset is discussed extensively in 3.1. Frame indices are represented by superscripts, where we assume that each sequence consists of $T + 1$ frames for simplicity. We note that it may be possible to roll-out predictions for multiple sequences autoregressively using techniques such as reconstruction guidance [18], but we leave exploration of this direction for future work. Our objective is to train a model to effectively *downscale*, or *super-resolve* a given sequence $\mathbf{x}^{0:T}$ with $\mathbf{y}^{0:T}$ serving as the target. Note we use both “downscaling” and “super-resolution” interchangeably.

More formally, let $\mathbf{x}^t \in \mathbb{R}^{C \times H \times W}$ and $\mathbf{y}^t \in \mathbb{R}^{1 \times sH \times sW}$ represent individual low-resolution and high-resolution frames. Here, $s \in \mathbb{N}$ denotes the downscaling factor, C represents the number of climate states used as input to the model, and H, W indicate the height and width of the low-resolution frame, respectively. For our study, we adopt an downscaling factor of $s = 8$ and have $C = 12$ total low-resolution channels. In addition to the low-resolution precipitation state, we provide an additional eleven channels of information to the model via concatenation, such as topography, wind velocity, and surface temperature; see Appendix A.2 for details.

2.0.2 Solution Sketch

We approach the downscaling problem as a conditional generative modeling task. Accordingly, we devise a model with the objective of learning conditional distribution of high-resolution precipitation frames, taking into account the contextual information provided by the low-resolution precipitation frame sequence.

Our proposed solution, **Spatiotemporal Video Diffusion (STVD)** (Fig. 1), relies on two modules: a deterministic downscaler based on spatio-temporal factorised attention and a stochastic component based on conditional diffusion models [17, 53], also leveraging factorised attention. The first module uses a UNet with spatio-temporal attention to integrate information from a low-resolution frame sequence. This process results in a high-resolution frame sequence, denoted by $\bar{\mathbf{y}}^{0:T}$, which serves as an initial prediction and is further refined by the second module. The second module is a conditional diffusion model that stochastically generates a sequence of additive residual frames $\mathbf{r}^{0:T}$ which serves to add fine-grained details to the initial prediction. In all, composing these two modules results in a predicted high-resolution frame sequence of the form $\hat{\mathbf{y}}^{0:T} = \bar{\mathbf{y}}^{0:T} + \mathbf{r}^{0:T}$. Both modules are trained end-to-end.

Decomposing the prediction target into a deterministic mean and a stochastic residual is inspired by recent findings in predictive-coding-based video decompression. Here, one aims to predict (in the best way possible) a sequence of video frames while compressing the sparse residuals [2, 64] that can be modeled more easily than dense frames. Similarly, it is easier to generate residuals than dense images when using diffusion models [63, 35].

In what follows, we first describe our overall probabilistic framework for downscaling. Then, we discuss the deterministic module along with temporal attention, followed by the remaining residual prediction module based on diffusion generative modeling. See Appendix A.1 for the details of our model architecture.

2.1 Probabilistic Modeling of Downscaling

Given a sequence of low-resolution frames $\mathbf{x}^{0:T}$ and the corresponding sequence of high-resolution frames $\mathbf{y}^{0:T}$, we seek to learn a parametric approximation p_θ of the underlying conditional distribution $p(\mathbf{y}^{0:T} | \mathbf{x}^{0:T}) \approx p_\theta(\mathbf{y}^{0:T} | \mathbf{x}^{0:T})$.

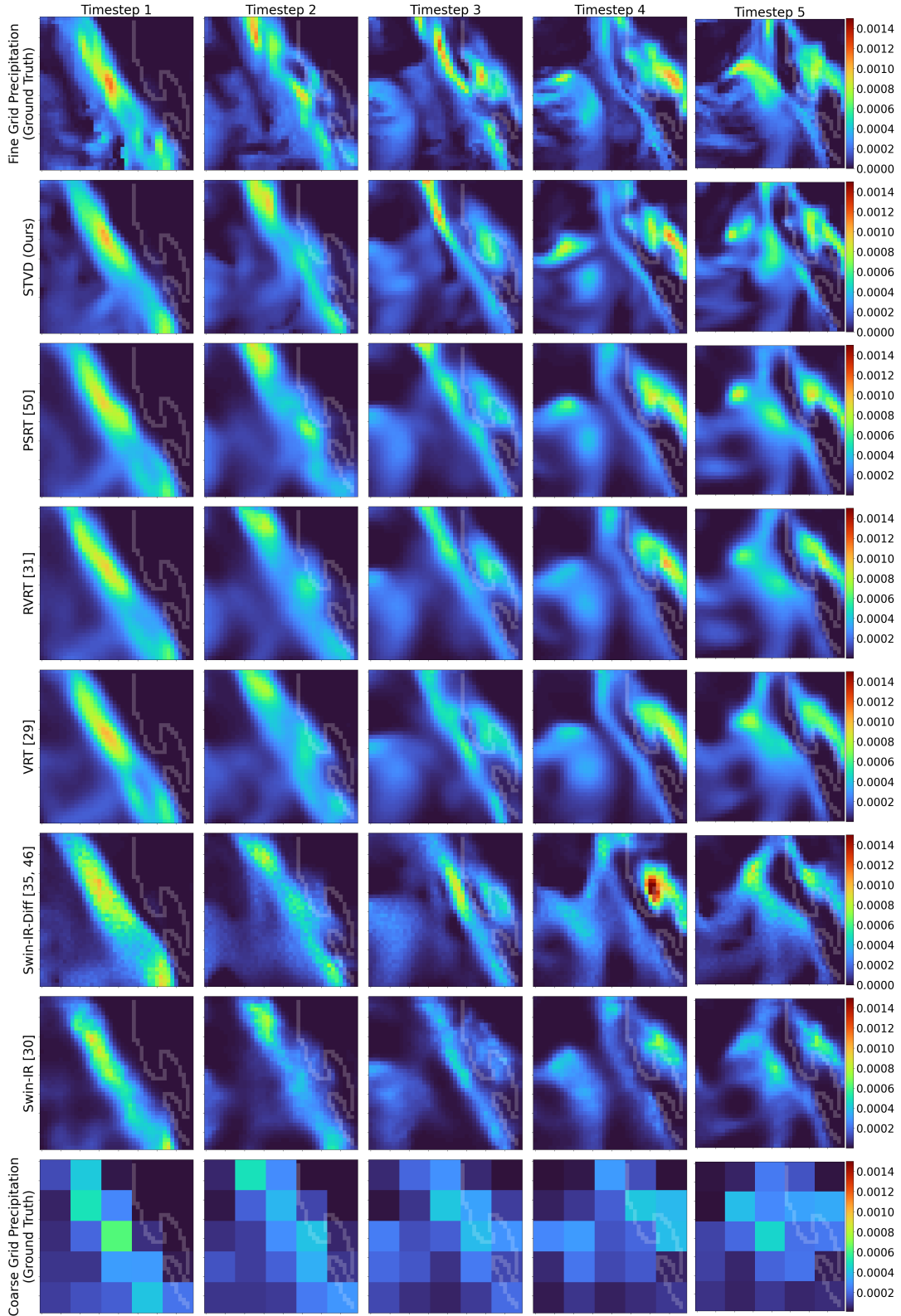


Figure 2: A qualitative comparison between our proposed model and baselines for a precipitation event associated with a cold front impinging on the Northern California coast and then the Sierra mountain range (coastline marked in hazy white). Fig. 4 plots the regional topography. The time interval between adjacent frames is 3 hours; the plotted region is 1000×1000 km. Our model resolves the fine-grid precipitation structure better than the considered baselines. See Appendix A.3 for additional samples.

Importantly, we make no independence assumptions across time, i.e. each generated frame \mathbf{y}^t is allowed to depend on all other generated frames. Moreover, the generated high-resolution frame sequence is conditioned on the entire low-resolution frame sequence. This allows us to capture any long-range temporal correlations between the frames, thereby enhancing the fidelity and cohesion of the high-resolution frame reconstruction.

As discussed in the overview of this section, the likelihood $p_\theta(\mathbf{y}^{0:T} | \mathbf{x}^{0:T})$ is modeled using a combination of a deterministic downscaler and a residual diffusion model. We will discuss how the model parameters $\theta = (\phi, \psi)$ decompose into those for a downscaler (ϕ) and a diffusion model (ψ).

2.1.1 Deterministic Downscaling

Our first module is a deterministic downscaler that predicts an initial high-resolution frame sequence

$$\bar{\mathbf{y}}^{0:T} = \mu_\phi(\mathbf{x}^{0:T}), \quad (1)$$

where μ_ϕ is a network generating a deterministic high-resolution prediction with parameters ϕ . We choose to perform bicubic interpolation on each frame of $\mathbf{x}^{0:T}$ before passing the frame sequence through the network μ_ϕ . As the diffusion network necessarily operates on high-resolution inputs (i.e. denoising the high-resolution residuals), this choice allows us to use the same UNet [42] architecture (with different weights) for both the downscaling module μ_ϕ and the residual diffusion module. This enables us to easily share features across the modules via concatenation. See Appendix A.1 for further details.

Importantly, μ_ϕ incorporates a temporal attention mechanism that allows any given frame at time t , or its corresponding feature map, to attend to all the context frames from 0 to T . This mechanism’s architecture allows for the concurrent inference of all frames within the sequence $\bar{\mathbf{y}}^{0:T}$. We emphasize that these attention weights are different for each frame, allowing for the flexible incorporation of information across time.

2.1.2 Stochastic Residual Modeling via Diffusion

After computing an initial high-resolution sequence $\bar{\mathbf{y}}^{0:T}$, the finer details that refine this prediction are modeled by residuals learned via a conditional diffusion model. That is, our final stochastic high-resolution frame sequence $\hat{\mathbf{y}}^{0:T}$ is generated by sampling an additive residual sequence $\mathbf{r}^{0:T}$ from a conditional diffusion model, i.e.

$$\hat{\mathbf{y}}^{0:T} = \bar{\mathbf{y}}^{0:T} + \mathbf{r}^{0:T}. \quad (2)$$

Thus, we seek to model the residuals $\mathbf{r}^{0:T} = \mathbf{y}^{0:T} - \bar{\mathbf{y}}^{0:T}$. We emphasize that our diffusion model generates the entire residual sequence $\mathbf{r}^{0:T}$ concurrently, with the generative process of residual \mathbf{r}^t dependent on the other residuals in the sequence. This is achieved via a UNet architecture with spatio-temporal attention, similar to the mechanism used for the deterministic downscaling module.

In order to model the distribution of $\mathbf{r}^{0:T}$, we leverage the framework of diffusion models, in particular the DDPM model [17]. To that end, we introduce a collection of latent variables $\mathbf{r}_{0:N}^{0:T}$, where the lower subscripts indicate the denoising diffusion step. In the *forward process* of a diffusion model, the latent variable $\mathbf{r}_n^{0:T}$ is created from $\mathbf{r}_{n-1}^{0:T}$ via additive noise. In the *reverse process*, which serves to perform generation, a denoising model (with parameters ψ) is trained to predict $\mathbf{r}_{j-1}^{0:T}$ from $\mathbf{r}_j^{0:T}$.

We use N to denote the total number of denoising steps. Note that $\mathbf{r}^{0:T} = \mathbf{r}_0^{0:T}$, i.e. the first diffusion step, corresponds to the true residual. We further note that $\mathbf{r}_0^{0:T}$ implicitly depends on the downscaler parameters ϕ , and hence we may simultaneously optimize all model parameters $\theta = (\phi, \psi)$ within the context of diffusion modeling.

As is standard in diffusion models [17], we parameterize the reverse process via a Gaussian distribution whose mean is determined by a neural network M_ψ ,

$$p_\psi(\mathbf{r}_{n-1}^{0:T} | \mathbf{r}_n^{0:T}, \mathbf{c}) = \mathcal{N}(\mathbf{r}_{n-1}^{0:T} | M_\psi(\mathbf{r}_n^{0:T}, n, \mathbf{c}), \gamma \mathbf{I}), \quad (3)$$

where M_ψ is a denoising network (a UNet with spatio-temporal attention). Here, the variance γ is a hyperparameter. We note that the diffusion model directly accesses the context $\mathbf{c} = (\mathbf{x}^{0:T}, \bar{\mathbf{y}}^{0:T})$, but is also implicitly conditioned on $\mathbf{x}^{0:T}$ via concatenation of feature maps from the downscaler module. As in the downscaler, we bicubically upsample $\mathbf{x}^{0:T}$ before channel-wise concatenation with $\bar{\mathbf{y}}^{0:T}$ to match the dimensions when forming \mathbf{c} .

Algorithm 1: Training STVD

```

while not converged do
    Sample  $\mathbf{x}^{0:T}$  and  $\mathbf{y}^{0:T}$ ;
     $n \sim \mathcal{U}(0, 1, 2, \dots, N)$ ;
     $\epsilon \sim \mathcal{N}(\mathbf{0}, \mathbf{I})$ ;
     $\bar{\mathbf{y}}^{0:T} = \mu_\phi(\mathbf{x}^{0:T})$ ;
     $\mathbf{r}_0^{0:T} = \mathbf{y}^{0:T} - \bar{\mathbf{y}}^{0:T}$ ;
     $\mathbf{v} = \alpha_n \epsilon - \sigma_n \mathbf{r}_0^{0:T}$ ;
     $\mathbf{r}_n^{0:T} = \alpha_n \mathbf{r}_0^{0:T} + \sigma_n \epsilon$ ;
     $\mathbf{c} = (\mathbf{x}^{0:T}, \bar{\mathbf{y}}^{0:T})$ ;
     $\hat{\mathbf{v}} = M_\psi(\mathbf{r}_n^{0:T}, n, \mathbf{c})$ ;
     $L = \|\mathbf{v} - \hat{\mathbf{v}}\|^2$ ;
     $(\psi, \phi) = (\psi, \phi) - \nabla_{\psi, \phi} L$ ;
    
```

Algorithm 2: Sampling STVD

```

Get an equally spaced increasing
sub-sequence  $\tau$  of  $[1, \dots, N]$  of
length  $S \ll N$ , i.e.,  $\{\tau_1, \dots, \tau_S\}$ ;
 $\bar{\mathbf{y}}^{0:T} = \mu_\phi(\mathbf{x}^{0:T})$ ;
 $\mathbf{c} = (\mathbf{x}^{0:T}, \bar{\mathbf{y}}^{0:T})$ ;
 $\mathbf{r}_S^{0:T} \sim \mathcal{N}(\mathbf{0}, \mathbf{I})$ ;
for  $n$  in reversed( $\tau$ ) do
     $\hat{\mathbf{v}} = M_\psi(\mathbf{r}_n^{0:T}, n, \mathbf{c})$ ;
     $\hat{\mathbf{r}} = \alpha_n \mathbf{r}_n^{0:T} - \sigma_n \hat{\mathbf{v}}$ ;
     $\hat{\epsilon} = \frac{\sigma_n}{\alpha_n}(\mathbf{r}_n^{0:T} - \hat{\mathbf{r}})$ ;
     $\mathbf{r}_{n-1}^{0:T} = \alpha_{n-1} \hat{\mathbf{r}} + \sigma_{n-1} \hat{\epsilon}$ ;
 $\hat{\mathbf{y}}^{0:T} = \bar{\mathbf{y}}^{0:T} + \mathbf{r}_0^{0:T}$ ;
    
```

2.1.3 Loss Function

To train our model, we use the angular parametrization suggested by [49]. More concretely, this results in the diffusion loss of the form

$$L(\psi, \phi) = \mathbb{E}_{\mathbf{x}^{0:T}, \mathbf{y}^{0:T}, n, \epsilon} \sum_{t=0}^T \|\mathbf{v} - M_\psi(\mathbf{r}_n^{0:T}, n, \mathbf{c})\|^2 \quad (4)$$

where $\epsilon \sim \mathcal{N}(0, I)$, n is sampled uniformly from $\{1, 2, \dots, N\}$, and the sequences $\mathbf{x}^{0:T}$, $\mathbf{y}^{0:T}$ are sampled from the training distribution. Note that $\mathbf{c} = (\mathbf{x}^{0:T}, \bar{\mathbf{y}}^{0:T})$ where $\bar{\mathbf{y}}^{0:T} = \mu_\phi(\mathbf{x}^{0:T})$. Here, the scalars $\alpha_n^2 = \prod_{i=1}^n (1 - \beta_i)$ and $\sigma_n^2 = 1 - \alpha_n^2$ are used to define $\mathbf{v} \equiv \alpha_n \epsilon - \sigma_n \mathbf{r}_0^{0:T}$.

Training and inference are concurrent across multiple frames by the inherent mechanism of spatio-temporal attention. Algorithm 1 and 2 demonstrate the training and sampling strategy under the angular parametrization. We use DDIM sampling [52] to generate frame residuals with fewer diffusion steps.

2.1.4 Network Architecture

Both the deterministic downscaler and the conditional diffusion model employ a UNet backbone (refer to Appendix A.1 for implementation details). The downscaler processes the multi-channel input frames ($\mathbf{x}^{0:T}$), yielding an initial estimate ($\bar{\mathbf{y}}^{0:T}$) focusing solely on the precipitation channel. The diffusion UNet, featuring similar architecture but with key adaptations, conditions on diffusion step n and concatenates feature maps from the downscaler with its own before every contraction in the UNet path. The channel concatenated input to the diffusion UNet ($\mathbf{x}^{0:T}$, $\bar{\mathbf{y}}^{0:T}$, and $\mathbf{r}_n^{0:T}$), along with the conditioning variables, i.e., diffusion step n and the feature maps from downscaler, yields the output \mathbf{v} .

Traditionally, most image diffusion models utilise a UNet architecture with convolutional residual blocks and transformer blocks [41]. Each transformer block contains a spatial self-attention and cross-attention. The spatial self-attention focuses on pixel correlations within feature maps, while cross-attention considers relationships between pixels and conditional inputs.

Temporal coherence in video data can be achieved by employing full attention across the entire three-dimensional data cube, encompassing spatial and temporal dimensions. However, the computational demands associated with this approach render it impractical for processing large sequences or high-resolution inputs. To optimize efficiency, we make several modifications. These include decoupling attention between spatial and temporal dimensions, utilizing a linear variant of self-attention [21] for non-bottleneck layers (where the effective number of “tokens” for attention is relatively large), focusing spatial attention on localized patches (instead of the entire feature map, which could be wasteful), and calculating per-channel temporal attention in large spatial dimensions (namely, the ultimate and penultimate expansion and contraction layers of UNet). These modifications dramatically reduce the time complexity and memory footprint of these transformer blocks. At each temporal attention block, the time dimension in the feature map tensor is ungrouped to facilitate inter-frame attention.

3 Experiments

We conduct a comprehensive evaluation of our proposed method, Spatiotemporal Video Diffusion (STVD), against five contemporary state-of-the-art baselines. The first two baselines are image super-resolution models based on the Swin

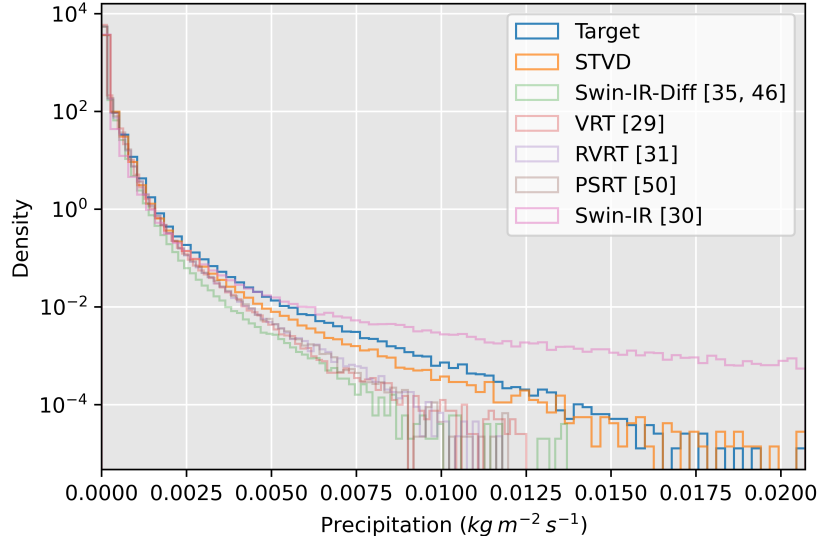


Figure 3: Distributions of the fine-grid three-hourly average precipitation, including all gridpoints around the globe. The Swin-IR baseline overestimates large precipitation events, whereas all other baselines underestimate key extreme and rare precipitation events. Our model aligns best with the fine-grid ground truth than any the other model. This is also evident with the the EMD and PE metrics discussed in Tab. 1 and Sec. 3.4.

Vision Transformer (Swin-IR)[30] and its residual diffusion variant (Swin-IR-Diff). The next two baselines are video super-resolution models grounded in vision transformer architecture (VRT) [29] and its recurrent variant (RVRT) [31]. The latter incorporates guided deformable attention for clip alignment, enhancing its temporal modeling capabilities. Lastly, we compare against another video-super-resolution baseline (PSRT) [50] which also relies on the transformer architecture but uses multi-frame attention groups.

We additionally perform ablation studies in three distinct configurations. In the first two ablations, we experiment with the input sequence length. While our proposed model uses a context length of 5 frames, we also conduct experiments with 3 frames and 1 frame (STVD-3 and STVD-1). Note that using a single context frame ablates for the temporal attention block as well. The third ablation (STVD-Single) involves removing the additional input channels (i.e. only providing the model with the low-resolution precipitation sequence) to assess their impact on performance metrics, providing valuable insights into the influence of these supplementary inputs on the model’s overall performance. In summary, our experiments demonstrate that our method outperforms all considered baselines across all metrics considered. Additionally, our ablation studies demonstrate the importance of temporal context and additional climate inputs.

3.1 Dataset

Our data derives from an 11-member initial condition ensemble of 13-month simulations using a global atmosphere model, FV3GFS, run at 25 km resolution, forced by climatological sea surface temperatures and sea ice. The first month of each simulation is discarded to allow the simulations to spin up and meteorologically diverge, effectively providing 11 years of reference data (of which first 10 years are used for training and the last year for validation). FV3GFS, developed by the National Oceanic and Atmospheric Administration (NOAA), is a version of NOAA’s operational global weather forecast model ([67, 7]).

Three-hourly average data were saved from this entire simulation, which was a 25 km horizontal “fine grid” (high-resolution frames). We further 8-fold coarsened the selected fields to a 200 km horizontal “coarse grid” to create paired data (x_t, y_t) , where x_t is the coarse-grid global state, and y_t is the corresponding fine-grid global state. Our goal is to apply video downscaling to the coarse-grid precipitation field to obtain temporally smooth fine-grid precipitation estimates that are statistically similar to the true data. This approach is attractive because many fine-grid precipitation features, such as cold fronts and tropical cyclones, are poorly resolved on the coarse grid but are temporally coherent across periods much longer than 3 hours. We use 12 coarse-grid input fields, including precipitation, topography, and horizontal vector wind at various levels. See Appendix A.2 for the list of included atmospheric variables. FV3GFS uses

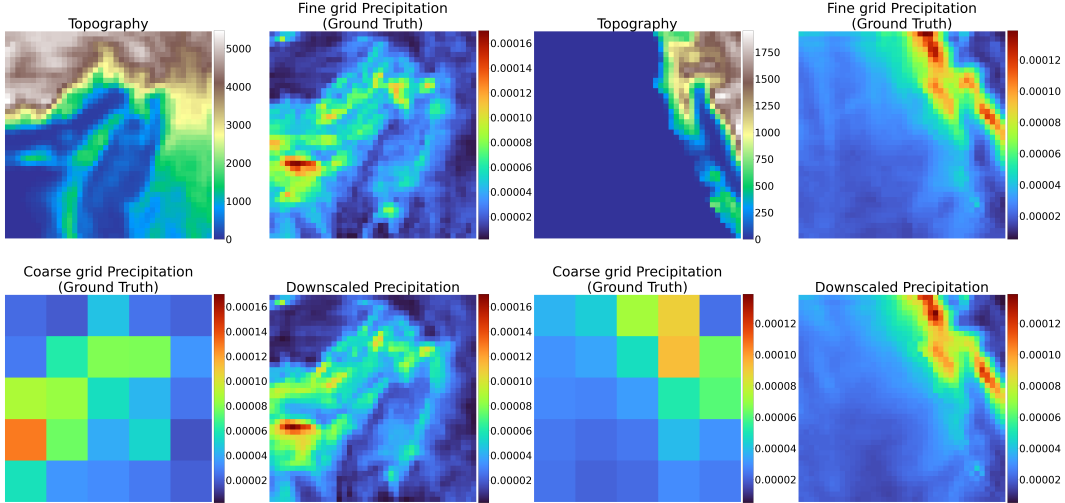


Figure 4: Precipitation over two different regions (left: Himalayas; right: Northern California coast, same region as Fig. 2), averaged across a year, for our STVD model and the ground-truth. For each half, the topography of the region is shown in the corresponding top-left whereas the predicted annual average is shown in the corresponding bottom-right. Annually-averaged precipitation is an important indicator of water availability in a region. STVD successfully captures many details of the precipitation that are tied to local topography and are too fine to be resolved the coarse-grid data.

a cubed-sphere grid, where the surface of the globe is divided into six tiles, each of which is covered by an $N \times N$ array of points. Our data fields reflect this structure with $N = 48$ for the 200 km coarse grid and $N = 384$ for the 25 km fine grid.

The application presented here is a pilot for broader applications of our methodology. Fine-grid simulations are much more computationally expensive than coarse-grid simulations (an 8-fold reduction in grid spacing requires almost 1000x more computation), so a coarse-grid simulation with super-resolved details in desired regions could be highly cost-effective for many applications.

During training, our VSR model randomly selects data at each time from one of the six tiles. This strategy ensures that the model learns from the diverse spatial contexts and weather regimes that produce precipitation in different parts of the world. Post-training, for localized analysis, we selectively sample super-resolved precipitation channels from regions with complex terrain, such as California. These regions can systematically pattern the precipitation on fine scales. This analysis helps us to see how well the super-resolution can learn the time-mean spatial patterns (e.g. precipitation enhancement on the windward side of mountain ranges and lee rain shadows) in the fine-grid reference data.

3.2 Training and Testing Details

We address the task of downscaling a sequence of precipitation frames with a scale factor of 8 applied to FV3GFS output. Our approach leverages a Spatiotemporal Video Diffusion (STVD) framework, which involves training on 5 consecutive frames, all of which are downscaled jointly.

We optimize our model using Adam [23] with an initial learning rate of 1×10^{-4} and cosine annealing with decay until 5×10^{-7} during training, executed on an NVidia RTX A6000 GPU. The diffusion model is trained using v-parametrization [49], with a fixed diffusion depth ($N = 1400$). Random tiles extracted from the cube-sphere representation of Earth, with dimensions 384 in high-resolution and 48 in low-resolution, are utilized during training. We train for one million steps, requiring approximately 7 days on a single node. We use a batch size of one, apply a logarithmic transformation to precipitation states, and normalize to the range $[-1, 1]$.

During testing, we employ DDIM sampling with 30 steps on an Exponential Moving Average (EMA) variant of our model, with a decay rate set to 0.995. Testing is conducted on the full frame size. A single diffusion loss optimises the entire pipeline end-to-end.

Table 1: Quantitative comparison between our STVD method and the various competitive baselines. EMD represents the Earth-Mover Distance, and PE denotes the 99.999th percentile error. Overall, our proposed method (STVD) outperforms the baselines across all metrics. The exclusion of additional side information (STVD-single) or decrement in context length (STVD-3 and STVD-1) appreciably degrades performance.

	CRPS (10^{-5})	MSE (10^{-8})	EMD (10^{-6})	PE (10^{-3})
STVD (ours)	1.85	0.59	2.49	1.2
PSRT [50]	2.15	0.66	4.21	3.8
RVRT [31]	3.55	1.73	4.33	3.6
VRT [29]	3.58	1.74	4.61	4.0
Swin-IR-Diff [35, 46]	2.29	1.94	6.38	4.4
Swin-IR [30]	2.36	2.29	17.40	23.40

STVD-single (ablation)	1.81	0.62	4.64	2.3
STVD-3 (ablation)	1.96	0.68	4.94	2.6
STVD-1 (ablation)	2.05	0.72	7.19	4.1

3.3 Baseline Models

We compare against several recent and high performing transformer-based video super-resolution models. These models are trained in a deterministic manner, thus allowing us to compare against our generative setup. The first, Video Restoration Transformer (VRT) [29], allows for parallel frame prediction and long-range temporal dependency modeling. The second, recurrent VRT (RVRT) [31], incorporates guided deformable attention for effective clip alignment, enhancing its temporal modeling capabilities. PSRT [50] removes the alignment module and modifies the attention window.

In addition, to assess the benefits of multi-frame downscaling, we compare to Swin-IR [30]. This model is a popular image super-resolution model that harnesses Swin Transformer blocks. Swin-IR is, however, still trained in a supervised fashion. Thus, as a generative baseline, we compare to Swin-IR-Diff. This model generates a deterministic prediction using Swin-IR [30], followed by modeling of a stochastic residual via diffusion. This baseline is inspired by concurrent work on single-image radar-reflectivity downscaling [35], where a UNet is used instead of Swin-IR. See Appendix A.2 for details.

3.4 Evaluation Metrics

We evaluate our model differently than for standard vision tasks. In addition to the Mean Square Error (MSE), which measures the average squared difference between predicted and actual values but does not capture the full distributional information, a more meaningful comparison includes several distribution-level metrics. One such important metric is the Continuous Ranked Probability Score (CRPS) [5, 56], used to assess the discrepancy between the predicted cumulative distribution function and the observed data. We compute CRPS over 10 stochastic realisations of our prediction for a give low-resolution sequence.

Furthermore, given the distinctive distribution of the precipitation climate state, characterized by a light-tailed exponential nature, it is important to ensure that the application of downscaling does not induce significant alterations in the distribution of precipitation rates. This gives rise to two additional metrics. First, we compute the Earth Mover Distance [44] to quantify the agreement between the target and predicted global precipitation distribution, which is strongly affected by high-resolution details. Second, focusing on tail events and extreme precipitation, we consider the 99.999th percentile error (PE) in the global precipitation distribution, providing a nuanced understanding of the model’s performance on rare and extreme precipitation events.

3.5 Qualitative and Quantitative Analysis

Tab. 1 presents a comprehensive quantitative evaluation comparing our method with state-of-the-art baselines and ablations. Our proposed model (STVD) exhibits strong performance across all metrics, outperforming all considered baselines. We highlight the distributional characteristics in Fig. 3. Swin-IR overestimates precipitation, whereas all other baselines underestimate precipitation. This is a highly undesirable property of a downscaling model, as poor performance on rare and extreme precipitation events can adversely affect marginal disaster mitigation policies. In

contrast, our method closely matches the precipitation distribution, as measured by the 99.999th percentile error and EMD.

The use of only precipitation as an input (STVD-single) results in slightly worse performance across all metrics, indicating that the additional inputs are indeed predictive. In contrast, our ablation model STVD-1, lacking the information from the full sequence, shows a significant difference, emphasizing the importance of temporal attention in our approach.

Fig. 2 depicts the performance of our model compared to other baselines on example of a precipitation feature interacting with mountainous terrain, using a three-hourly succession of plots. A cold front (linear feature in the left-most column of plots) impinges on northern California, producing enhanced precipitation first over the coastal foothills and then over the northwest-southeast ridge of the Sierra mountain range in the lower right corner of the images. Our model generates high quality results which preserves most patterns with a high degree of similarity. RVRT produces slightly more diffuse precipitation features, while Swin-IR produces slightly more pixelated precipitation features.

Fig. 4 shows annually-averaged precipitation from the patch in Fig. 2. Accurately capturing the fine-grid structure of time-mean precipitation is an informative metric and important for assessing long-term water availability. Our method (which includes fine-grid topography as a training input) is remarkably successful in replicating the ground truth, including the strength and narrow spatial structure of the bands of high precipitation along the Northern California coastal mountains and the Sierras. These features are not resolved by the coarse-grid inputs to the super-resolution. Appendix A.3 has additional samples.

4 Related Work

Diffusion Models Diffusion models [51, 17, 59, 53, 54] are a class of generative models which generate data via an iterative denoising process. Most closely related to our work are diffusion models for video. Recent models [63] propose to generate deterministic next-frame predictions autoregressively with additional residuals generated by a diffusion model, or generate videos directly via diffusion [15].

Image Super-Resolution Single image super-resolution is a challenging and important task in computer vision [61]. While there exist many classical approaches to this problem [4, 10], deep learning based methods have recently become the dominant paradigm [61]. Supervised approaches are typical, where models are trained to minimize the error between generated and ground-truth images [65, 8, 30]. On the other hand, generative approaches [36, 46, 3] model the data distribution itself, often leading to higher quality outputs. In particular, cascaded diffusion models [39, 45] and SR3 [46] propose models for single image super-resolution but are unable to leverage the temporal context.

Video Super-Resolution Many approaches for video super-resolution not based on diffusion models [6, 11, 19]. We refer to [33] for a more comprehensive overview. The recent VRT model [29] is a transformer-based model for video super-resolution with a recurrent variant RVRT [32] that focuses on parallel decoding and guided clip alignment. We note that these state-of-the-art approaches are deterministic, whereas our approach is generative, allowing us to directly model the (conditional) data distribution, thus preventing mode averaging.

Data-driven weather and climate modeling Advancements in climate data processing and downscaling have prominently featured the application of CNNs. [58] draw inspiration from FRVSR [47], adopting an iterative approach that utilizes the high-resolution frame estimated in the previous step as input for subsequent iterations. [62] employed Fourier neural operators for versatile downscaling. [13] contribute by generating physically consistent downscaled climate states, employing a softmax layer to enforce conservation laws.

A concurrent work [35] employs diffusion models for downscaling of climate states at each time point. The use of GANs has also been pervasive in downscaling and precipitation prediction, as extensively reviewed in recent literature [27, 38, 14, 40, 12, 60]. Beyond downscaling, [1] demonstrate the diffusion model’s efficacy in synthesizing full rain density from vorticity inputs. Additionally, [16] uses a diffusion model for downscaling solar irradiance. These models are also used for probabilistic weather forecasting and nowcasting [26, 28].

5 Conclusion

We propose a video super-resolution method for probabilistic precipitation downscaling. Our model, STVD, operates by deterministically super-resolving a given low-resolution frame sequence, followed by stochastically modeling the residual details via diffusion. Our model successfully resolves how fine-grid precipitation features, generated as weather

systems, interact with complex coastlines and mountains based on temporally coherent coarse-grid information. Our method outperforms several competitive baselines on a range of quantitative metrics. This is an important step towards designing effective statistical downscaling methods to provide highly localized information about planning for extreme weather events, such as floods or hurricanes in a warming climate, based on computationally tractable coarse-grid atmospheric models.

Acknowledgements We thank Kushagra Pandey and Yibo Yang for valuable feedback. Prakhar Srivastava was supported by the Allen Institute for AI summer internship for much of this work. Stephan Mandt acknowledges support from the National Science Foundation (NSF) under an NSF CAREER Award, award numbers 2003237 and 2007719, by the Department of Energy under grant DE-SC0022331, by the IARPA WRIVA program, and by gifts from Qualcomm and Disney. Gavin Kerrigan is supported in part by the HPI Research Center in Machine Learning and Data Science at UC Irvine.

References

- [1] Addison, H., Kendon, E., Ravuri, S., Aitchison, L., Watson, P.A.: Machine learning emulation of a local-scale uk climate model. arXiv preprint arXiv:2211.16116 (2022)
- [2] Agustsson, E., Minnen, D., Johnston, N., Balle, J., Hwang, S.J., Toderici, G.: Scale-space flow for end-to-end optimized video compression. In: Proceedings of the IEEE/CVF Conference on Computer Vision and Pattern Recognition. pp. 8503–8512 (2020)
- [3] Andrei, S.S., Shapovalova, N., Mayol-Cuevas, W.: SUPERVEGAN: Super resolution video enhancement GAN for perceptually improving low bitrate streams. IEEE Access **9**, 91160–91174 (2021)
- [4] Bascle, B., Blake, A., Zisserman, A.: Motion deblurring and super-resolution from an image sequence. In: Computer Vision—ECCV’96: 4th European Conference on Computer Vision Cambridge, UK, April 15–18, 1996 Proceedings Volume II 4. pp. 571–582. Springer (1996)
- [5] Brown, T.A.: Admissible scoring systems for continuous distributions. (1974)
- [6] Chan, K.C., Wang, X., Yu, K., Dong, C., Loy, C.C.: Basicvsr: The search for essential components in video super-resolution and beyond. In: Proceedings of the IEEE/CVF Conference on Computer Vision and Pattern Recognition. pp. 4947–4956 (2021)
- [7] Community, U.: Ufs weather model (Jan 2021). doi:10.5281/zenodo.4460292, <https://doi.org/10.5281/zenodo.4460292>
- [8] Dai, T., Cai, J., Zhang, Y., Xia, S.T., Zhang, L.: Second-order attention network for single image super-resolution. In: Proceedings of the IEEE/CVF conference on computer vision and pattern recognition. pp. 11065–11074 (2019)
- [9] Dong, C., Loy, C.C., He, K., Tang, X.: Image super-resolution using deep convolutional networks. IEEE Transactions on Pattern Analysis and Machine Intelligence **38**(2), 295–307 (2015)
- [10] Farsiu, S., Robinson, M.D., Elad, M., Milanfar, P.: Fast and robust multiframe super resolution. IEEE transactions on image processing **13**(10), 1327–1344 (2004)
- [11] Fuoli, D., Gu, S., Timofte, R.: Efficient video super-resolution through recurrent latent space propagation. In: 2019 IEEE/CVF International Conference on Computer Vision Workshop (ICCVW). pp. 3476–3485. IEEE (2019)
- [12] Gong, A., Li, R., Pan, B., Chen, H., Ni, G., Chen, M.: Enhancing spatial variability representation of radar nowcasting with generative adversarial networks. Remote Sensing **15**(13), 3306 (2023)
- [13] Harder, P., Yang, Q., Ramesh, V., Sattigeri, P., Hernandez-Garcia, A., Watson, C., Szwarcman, D., Rolnick, D.: Generating physically-consistent high-resolution climate data with hard-constrained neural networks. arXiv preprint arXiv:2208.05424 (2022)
- [14] Harris, L., McRae, A.T., Chantry, M., Dueben, P.D., Palmer, T.N.: A generative deep learning approach to stochastic downscaling of precipitation forecasts. Journal of Advances in Modeling Earth Systems **14**(10), e2022MS003120 (2022)
- [15] Harvey, W., Naderiparizi, S., Masrani, V., Weillbach, C.D., Wood, F.: Flexible diffusion modeling of long videos. In: Advances in Neural Information Processing Systems (2022)
- [16] Hatanaka, Y., Glaser, Y., Galgon, G., Torri, G., Sadowski, P.: Diffusion models for high-resolution solar forecasts. arXiv preprint arXiv:2302.00170 (2023)
- [17] Ho, J., Jain, A., Abbeel, P.: Denoising diffusion probabilistic models. Advances in Neural Information Processing Systems **33**, 6840–6851 (2020)

- [18] Ho, J., Salimans, T., Gritsenko, A., Chan, W., Norouzi, M., Fleet, D.J.: Video diffusion models. arXiv preprint arXiv:2204.03458 (2022)
- [19] Huang, Y., Wang, W., Wang, L.: Bidirectional recurrent convolutional networks for multi-frame super-resolution. *Advances in neural information processing systems* **28** (2015)
- [20] Kappeler, A., Yoo, S., Dai, Q., Katsaggelos, A.K.: Video super-resolution with convolutional neural networks. *IEEE transactions on computational imaging* **2**(2), 109–122 (2016)
- [21] Katharopoulos, A., Vyas, A., Pappas, N., Fleuret, F.: Transformers are rnns: Fast autoregressive transformers with linear attention. In: *International conference on machine learning*. pp. 5156–5165. PMLR (2020)
- [22] Kim, J., Lee, J.K., Lee, K.M.: Accurate image super-resolution using very deep convolutional networks. In: *Proceedings of the IEEE conference on computer vision and pattern recognition*. pp. 1646–1654 (2016)
- [23] Kingma, D.P., Ba, J.: Adam: A method for stochastic optimization. arXiv preprint arXiv:1412.6980 (2014)
- [24] Lam, R., Sanchez-Gonzalez, A., Willson, M., Wyrnsberger, P., Fortunato, M., Alet, F., Ravuri, S., Ewalds, T., Eaton-Rosen, Z., Hu, W., et al.: Learning skillful medium-range global weather forecasting. *Science* **382**(6677), 1416–1421 (2023)
- [25] Ledig, C., Theis, L., Huszár, F., Caballero, J., Cunningham, A., Acosta, A., Aitken, A., Tejani, A., Totz, J., Wang, Z., et al.: Photo-realistic single image super-resolution using a generative adversarial network. In: *Proceedings of the IEEE conference on computer vision and pattern recognition*. pp. 4681–4690 (2017)
- [26] Leinonen, J., Hamann, U., Nerini, D., Germann, U., Franch, G.: Latent diffusion models for generative precipitation nowcasting with accurate uncertainty quantification. arXiv preprint arXiv:2304.12891 (2023)
- [27] Leinonen, J., Nerini, D., Berne, A.: Stochastic super-resolution for downscaling time-evolving atmospheric fields with a generative adversarial network. *IEEE Transactions on Geoscience and Remote Sensing* **59**(9), 7211–7223 (2020)
- [28] Li, L., Carver, R., Lopez-Gomez, I., Sha, F., Anderson, J.: Seeds: Emulation of weather forecast ensembles with diffusion models. arXiv preprint arXiv:2306.14066 (2023)
- [29] Liang, J., Cao, J., Fan, Y., Zhang, K., Ranjan, R., Li, Y., Timofte, R., Van Gool, L.: Vrt: A video restoration transformer. arXiv preprint arXiv:2201.12288 (2022)
- [30] Liang, J., Cao, J., Sun, G., Zhang, K., Van Gool, L., Timofte, R.: Swinir: Image restoration using swin transformer. In: *Proceedings of the IEEE/CVF international conference on computer vision*. pp. 1833–1844 (2021)
- [31] Liang, J., Fan, Y., Xiang, X., Ranjan, R., Ilg, E., Green, S., Cao, J., Zhang, K., Timofte, R., Gool, L.V.: Recurrent video restoration transformer with guided deformable attention. *Advances in Neural Information Processing Systems* **35**, 378–393 (2022)
- [32] Liang, J., Fan, Y., Xiang, X., Ranjan, R., Ilg, E., Green, S., Cao, J., Zhang, K., Timofte, R., Van Gool, L.: Recurrent video restoration transformer with guided deformable attention. In: *Advances in Neural Information Processing Systems* (2022)
- [33] Liu, H., Ruan, Z., Zhao, P., Dong, C., Shang, F., Liu, Y., Yang, L., Timofte, R.: Video super-resolution based on deep learning: a comprehensive survey. *Artificial Intelligence Review* **55**(8), 5981–6035 (2022)
- [34] Mahecha, M.D., Gans, F., Brandt, G., Christiansen, R., Cornell, S.E., Fomferra, N., Kraemer, G., Peters, J., Bodesheim, P., Camps-Valls, G., et al.: Earth system data cubes unravel global multivariate dynamics. *Earth System Dynamics* **11**(1), 201–234 (2020)
- [35] Mardani, M., Brenowitz, N., Cohen, Y., Pathak, J., Chen, C.Y., Liu, C.C., Vahdat, A., Kashinath, K., Kautz, J., Pritchard, M.: Generative residual diffusion modeling for km-scale atmospheric downscaling. arXiv preprint arXiv:2309.15214 (2023)
- [36] Menon, S., Damian, A., Hu, S., Ravi, N., Rudin, C.: Pulse: Self-supervised photo upsampling via latent space exploration of generative models. In: *Proceedings of the IEEE/CVF conference on computer vision and pattern recognition*. pp. 2437–2445 (2020)
- [37] Pathak, J., Subramanian, S., Harrington, P., Raja, S., Chattopadhyay, A., Mardani, M., Kurth, T., Hall, D., Li, Z., Azizzadenesheli, K., et al.: Fourcastnet: A global data-driven high-resolution weather model using adaptive fourier neural operators. arXiv preprint arXiv:2202.11214 (2022)
- [38] Price, I., Rasp, S.: Increasing the accuracy and resolution of precipitation forecasts using deep generative models. In: *International conference on artificial intelligence and statistics*. pp. 10555–10571. PMLR (2022)
- [39] Ramesh, A., Dhariwal, P., Nichol, A., Chu, C., Chen, M.: Hierarchical text-conditional image generation with CLIP latents. arXiv preprint arXiv:2204.06125 (2022)

- [40] Ravuri, S., Lenc, K., Willson, M., Kangin, D., Lam, R., Mirowski, P., Fitzsimons, M., Athanassiadou, M., Kashem, S., Madge, S., et al.: Skilful precipitation nowcasting using deep generative models of radar. *Nature* **597**(7878), 672–677 (2021)
- [41] Rombach, R., Blattmann, A., Lorenz, D., Esser, P., Ommer, B.: High-resolution image synthesis with latent diffusion models. In: Proceedings of the IEEE/CVF conference on computer vision and pattern recognition. pp. 10684–10695 (2022)
- [42] Ronneberger, O., Fischer, P., Brox, T.: U-net: Convolutional networks for biomedical image segmentation. In: Medical Image Computing and Computer-Assisted Intervention–MICCAI 2015: 18th International Conference, Munich, Germany, October 5-9, 2015, Proceedings, Part III 18. pp. 234–241. Springer (2015)
- [43] Rota, C., Buzzelli, M., Bianco, S., Schettini, R.: Video restoration based on deep learning: a comprehensive survey. *Artificial Intelligence Review* pp. 1–48 (2022)
- [44] Rubner, Y., Tomasi, C., Guibas, L.J.: A metric for distributions with applications to image databases. In: Sixth international conference on computer vision (IEEE Cat. No. 98CH36271). pp. 59–66. IEEE (1998)
- [45] Saharia, C., Chan, W., Saxena, S., Li, L., Whang, J., Denton, E., Ghasemipour, S.K.S., Gontijo-Lopes, R., Ayan, B.K., Salimans, T., Ho, J., Fleet, D.J., Norouzi, M.: Photorealistic text-to-image diffusion models with deep language understanding. In: Advances in Neural Information Processing Systems (2022)
- [46] Saharia, C., Ho, J., Chan, W., Salimans, T., Fleet, D.J., Norouzi, M.: Image super-resolution via iterative refinement. *IEEE Transactions on Pattern Analysis and Machine Intelligence* pp. 1–14 (2022)
- [47] Sajjadi, M.S., Vemulapalli, R., Brown, M.: Frame-recurrent video super-resolution. In: Proceedings of the IEEE conference on computer vision and pattern recognition. pp. 6626–6634 (2018)
- [48] Salathé, E.P., Steed, R., Mass, C.F., Zahn, P.H.: A high-resolution climate model for the us pacific northwest: Mesoscale feedbacks and local responses to climate change. *Journal of climate* **21**(21), 5708–5726 (2008)
- [49] Salimans, T., Ho, J.: Progressive distillation for fast sampling of diffusion models. *ArXiv* **abs/2202.00512** (2022)
- [50] Shi, S., Gu, J., Xie, L., Wang, X., Yang, Y., Dong, C.: Rethinking alignment in video super-resolution transformers. *Advances in Neural Information Processing Systems* **35**, 36081–36093 (2022)
- [51] Sohl-Dickstein, J., Weiss, E., Maheswaranathan, N., Ganguli, S.: Deep unsupervised learning using nonequilibrium thermodynamics. In: International Conference on Machine Learning. pp. 2256–2265 (2015)
- [52] Song, J., Meng, C., Ermon, S.: Denoising diffusion implicit models. *arXiv preprint arXiv:2010.02502* (2020)
- [53] Song, Y., Ermon, S.: Generative modeling by estimating gradients of the data distribution. *Advances in Neural Information Processing Systems* **32** (2019)
- [54] Song, Y., Sohl-Dickstein, J., Kingma, D.P., Kumar, A., Ermon, S., Poole, B.: Score-based generative modeling through stochastic differential equations. In: International Conference on Learning Representations (2021)
- [55] Stevens, B., Satoh, M., Auger, L., Biercamp, J., Bretherton, C.S., Chen, X., Düben, P., Judt, F., Khairoutdinov, M., Klocke, D., et al.: Dyamond: the dynamics of the atmospheric general circulation modeled on non-hydrostatic domains. *Progress in Earth and Planetary Science* **6**(1), 1–17 (2019)
- [56] Taillardat, M., Fougères, A.L., Naveau, P., De Fondeville, R.: Evaluating probabilistic forecasts of extremes using continuous ranked probability score distributions. *International Journal of Forecasting* **39**(3), 1448–1459 (2023)
- [57] Tang, J., Niu, X., Wang, S., Gao, H., Wang, X., Wu, J.: Statistical downscaling and dynamical downscaling of regional climate in china: Present climate evaluations and future climate projections. *Journal of Geophysical Research: Atmospheres* **121**(5), 2110–2129 (2016)
- [58] Teufel, B., Carmo, F., Sushama, L., Sun, L., Khaliq, M., Bélair, S., Shamseldin, A., Kumar, D.N., Vaze, J.: Physics-informed deep learning framework to model intense precipitation events at super resolution. *Geoscience Letters* **10**(1), 19 (2023)
- [59] Vincent, P.: A connection between score matching and denoising autoencoders. *Neural Computation* **23**(7), 1661–1674 (2011)
- [60] Vosper, E., Watson, P., Harris, L., McRae, A., Santos-Rodriguez, R., Aitchison, L., Mitchell, D.: Deep learning for downscaling tropical cyclone rainfall to hazard-relevant spatial scales. *Journal of Geophysical Research: Atmospheres* p. e2022JD038163 (2023)
- [61] Wang, Z., Chen, J., Hoi, S.C.: Deep learning for image super-resolution: A survey. *IEEE transactions on pattern analysis and machine intelligence* **43**(10), 3365–3387 (2020)

- [62] Yang, Q., Hernandez-Garcia, A., Harder, P., Ramesh, V., Sattegeri, P., Szwarcman, D., Watson, C.D., Rolnick, D.: Fourier neural operators for arbitrary resolution climate data downscaling. arXiv preprint arXiv:2305.14452 (2023)
- [63] Yang, R., Srivastava, P., Mandt, S.: Diffusion probabilistic modeling for video generation. *Entropy* **25**(10), 1469 (2023)
- [64] Yang, R., Yang, Y., Marino, J., Mandt, S.: Insights from generative modeling for neural video compression. *IEEE Transactions on Pattern Analysis and Machine Intelligence* (2023)
- [65] Zhang, Y., Li, K., Li, K., Wang, L., Zhong, B., Fu, Y.: Image super-resolution using very deep residual channel attention networks. In: *Proceedings of the European conference on computer vision (ECCV)*. pp. 286–301 (2018)
- [66] Zhao, S., Song, J., Ermon, S.: Towards deeper understanding of variational autoencoding models. arXiv preprint arXiv:1702.08658 (2017)
- [67] Zhou, L., Lin, S.J., Chen, J.H., Harris, L.M., Chen, X., Rees, S.L.: Toward convective-scale prediction within the next generation global prediction system. *Bulletin of the American Meteorological Society* **100**(7), 1225–1243 (2019)

Precipitation Downscaling with Spatiotemporal Video Diffusion

Supplementary Materials

A.1 Model Architecture

Our architecture is a conditional extension of the DDPM [17] and SR3 [46] models. As discussed in Sec. 2, Fig. 5 outlines the architecture of the proposed *denoising* and *downscaling* networks. Furthermore, Fig. 6 outlines the detail of each box. Before elaborating on the details, we define the naming convention for the parameter choices that we adopt in this section:

- **ChannelDim**: ResBlock channel dimension for first contractive layer of UNet.
- **ChannelMultipliers**: channel dimension multipliers for subsequent contractive layers (including the first layer) in both the downscaling and denoising modules. The expansive layer multipliers follow in reverse.
- **ResBlock**: leverages a standard implementation of ResBlock, i.e., two blocks each with a weight-standardised convolution of 3×3 kernel, Group Normalization over groups of 8 and SiLU activation, followed by a channel-adjusting 1×1 convolution.
- **Attention**: leverages standard implementation of quadratic or linear attention, incorporating 4 attention heads, each with a 32-dimensional representation. Utilizing a 3×3 convolutional kernel, query, key, and value feature maps are generated, resulting in feature maps of size $[B \times T, H \times C, X, Y]$, where B, T, C, X, and Y denote batch, time, channel, height, and width, respectively, with H representing the number of heads. These feature maps undergo rearrangement to the form $[BATCH, HEAD, CHANNEL, TOKEN]$, facilitating self-attention between TOKENS of CHANNEL dimensions. The chosen rearrangement order determines whether spatial or temporal self-attention is performed. Subsequently, the feature maps revert to their original format, upon which a separate convolution operation is conducted, followed by layer normalization to project the feature maps back to their original dimensions, akin to their state before the initial convolution within the attention block. Further elaboration on the rearrangement choices for the variants is discussed, adhering to *einops*⁹ notation:
 - **Q-Spatial**: quadratic variant, applied in the bottleneck layer, self attends between every pixel of the feature map with the following rearrangement : $[B \times T, H \times C, X, Y] \rightarrow [B \times T, H, C, X \times Y]$
 - **Q-Temporal**: quadratic variant, applied in the bottleneck layer, self attends between feature maps across time with the following rearrangement : $[B \times T, H \times C, X, Y] \rightarrow [B, H, C \times X \times Y, T]$
 - **L-Spatial**: linear variant, applied in expansive and contractive layers of UNet, self attends between every pixel within a patch of the feature map with the following rearrangement : $[B \times T, H \times C, X \times P, Y \times P] \rightarrow [B \times T, H \times X \times Y, C, P \times P]$ where P is patch size, starting with 192, halving at each contractive layer and doubling at each expansive layer.
 - **L-Temporal**: linear variant, applied in expansive and contractive layers of UNet, self attends between feature maps across time in a channel factorised manner with the following rearrangement : $[B \times T, H \times C, X, Y] \rightarrow [B, H \times X \times Y, C, T]$
- **MLP**: conditioning on the denoising step n is achieved through this block which uses 32-dimensional random Fourier features, followed a linear layer, GELU activation and another linear layer to transform the noise step to a higher dimension.
- **Cov/TransCov**: these are convolutional (3×3 kernel) downsampling and upsampling blocks that change the spatial size by a factor of 2.

Fig. 5 shows how the U-Net from both the denoising and downscaling networks interact with each other. The top U-Net depicts the denoising network whereas the bottom U-Net depicts the downscaling network. The denoising network is conditioned in three ways. First, the network is conditioned on the bicubically downscaled low-resolution frame $\mathbf{x}^{0:T}$ and concatenating it with both $\mathbf{r}_n^{0:T}$ (noisy residual) and $\bar{\mathbf{y}}^{0:T}$ (downscaler output) along the channel dimension. Second, the network is also conditioned on the feature maps generated by the downscaler network (see Eq. 1 and Eq. 3) as shown via the green arrows connecting the downsampling units of both the networks. As detailed in the figure, L-(Spatial/Temporal) Attention blocks from contractive layers of the downscaler network yield a feature map

⁹<https://einops.rocks/1-einops-basics/>

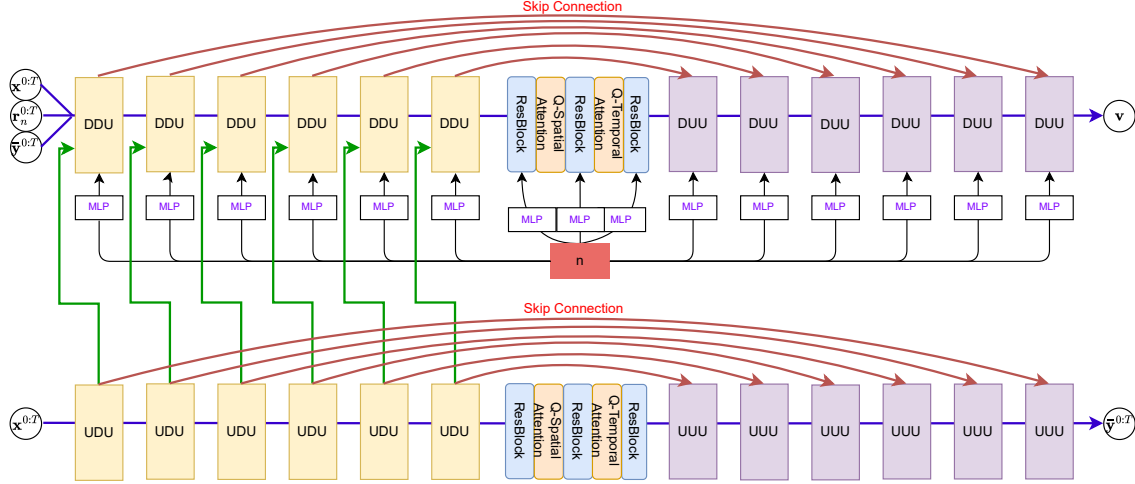


Figure 5: The figure depicts the overall model architecture where the top UNet performs diffusion on the residual, conditioned on the noise step n , $\mathbf{x}^{0:T}$, $\bar{\mathbf{y}}^{0:T}$ and the context of the bottom U-Net feature map (refer to Eq. 3 in Sec. 2.1). The bottom UNet is the deterministic downscaler (Eq. 1). Details of each block are shown in Fig. 6.

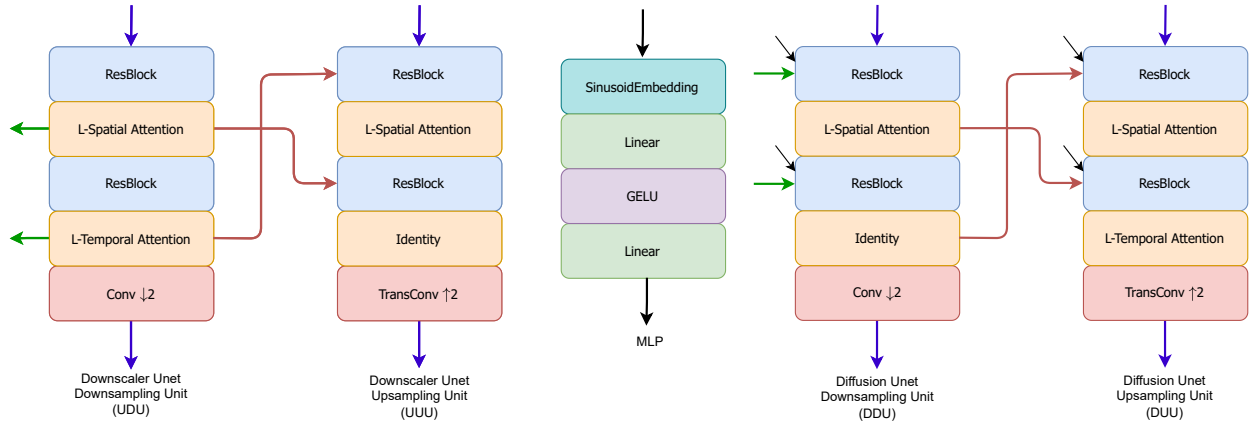


Figure 6: The details of the components of the modules shown in Fig. 5; the colored arrows in the modules correspond to the arrows with the same color in Fig. 5.

that gets concatenated along the inputs of both ResBlocks of the contractive layer of the denoising network. Finally, each contractive and expansive layer of the diffusion UNet gets conditioned on the denoising step n as shown via the **black** arrows. This conditional embedding for the step is generated through MLP. As shown in the Figure, this embedding is received by both ResBlocks. The information flows from the noisy residual through the network, as shown via **blue** arrows to predict the angular parameter \mathbf{v} . Both U-Nets have skip connections (shown via **red** arrows) between both ResBlocks of contractive and expansive layers of the same UNet.

TileSize	ChannelDim	ChannelMultipliers
384×384	64	1,1,2,2,3,4

Table 2: FV3GFS uses a cubed-sphere grid, in which the surface of the globe is divided into six tiles. A single high-resolution tile covers 25km and is 384×384 . Our UNet Encoder and Decoder has 6 layers with a base channel dimension of 64 and multipliers as stated above.

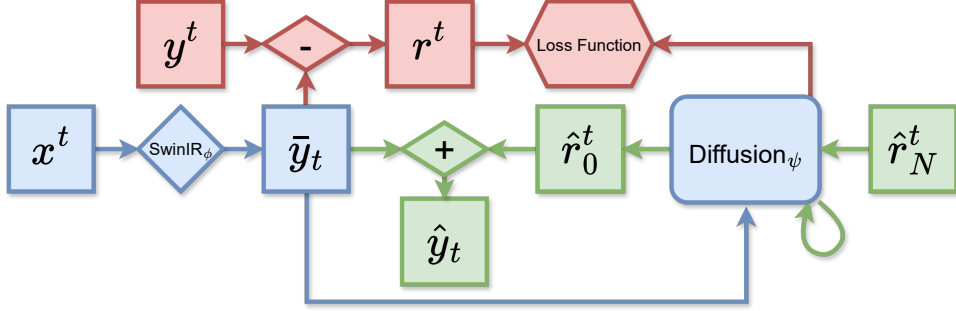


Figure 7: An illustration of the training and inference pipelines of Swin-IR-Diff. Similar to Fig. 1, blue blocks represent operations common to both training and inference phases. Red blocks signify operations exclusive to training, while green blocks indicate inference-only processes. However, in a major contrast, it is an image-only downscaler. In summary, this model takes in a current low-resolution frame which is deterministically downscaled via Swin-IR, followed by modeling of the residual details via conditional diffusion. The model details remain similar to what is described in Appendix A.1 with the absence of downscaler-conditioning and temporal attention in the diffusion model.

Table 3: Additional Variables in FV3GFS dataset.

Short Name	Long Name	Units
CPRATsfc	Surface convective precip. rate	kg/m ² /s
DSWRFtoa	Top of atmos. down shortwave flux	W/m ²
TMPsfc	Surface temperature	K
UGRD10m	10-meter eastward wind	m/s
VGRD10m	10-meter northward wind	m/s
ps	Surface pressure	Pa
u700	700-mb eastward wind	m/s
v700	700-mb northward wind	m/s
liq_wat	Vert. integral of cloud water mix ratio	kg/kg kg/m ²
sphum	Vert. integral of specific humidity	kg/kg kg/m ²
zsurf	Topography	–

A.2 On Swin-IR-Diff and Multiple Channels

Here, we discuss SwinIR-Diff, which expands on one of our robust baselines. Sec. 3.3 provides a concise overview of Swin-IR-Diff. Shown as a sketch in Fig. 7, this model opts to downscale each precipitation state individually, akin to an image super-resolution model. Resembling SR3 in its foundation of a conditional diffusion model, Swin-IR-Diff adopts a residual pipeline. It involves a deterministic prediction corrected by a residual generated from the conditional diffusion model, with the Swin-IR model serving as the deterministic downscaler in this context.

We conducted an ablation, focusing on the incorporation of additional climate states as input to our precipitation downscaling model STVD. The rationale for including these states is drawn from the insights of [14], who justified a similar selection for the task of precipitation forecast based on domain science. While Tab. 3 provides detailed information on the various states employed, the utility of these states is closely examined in Tab. 1, with specific attention to STVD (multiple input states) and STVD-single (only precipitation state as input). Clearly, the introduction of additional channels yields a notable improvement in performance.

A.3 Additional Samples

In addition to illustrating precipitation downscaling in the Sierras and Central California, we present our model’s output for another unique region—the Himalayas. Fig. 8 mirrors Fig. 2, displaying outputs from different models. Note that for the same regional topography, Fig. 4 (left) compares the annual precipitation time average.

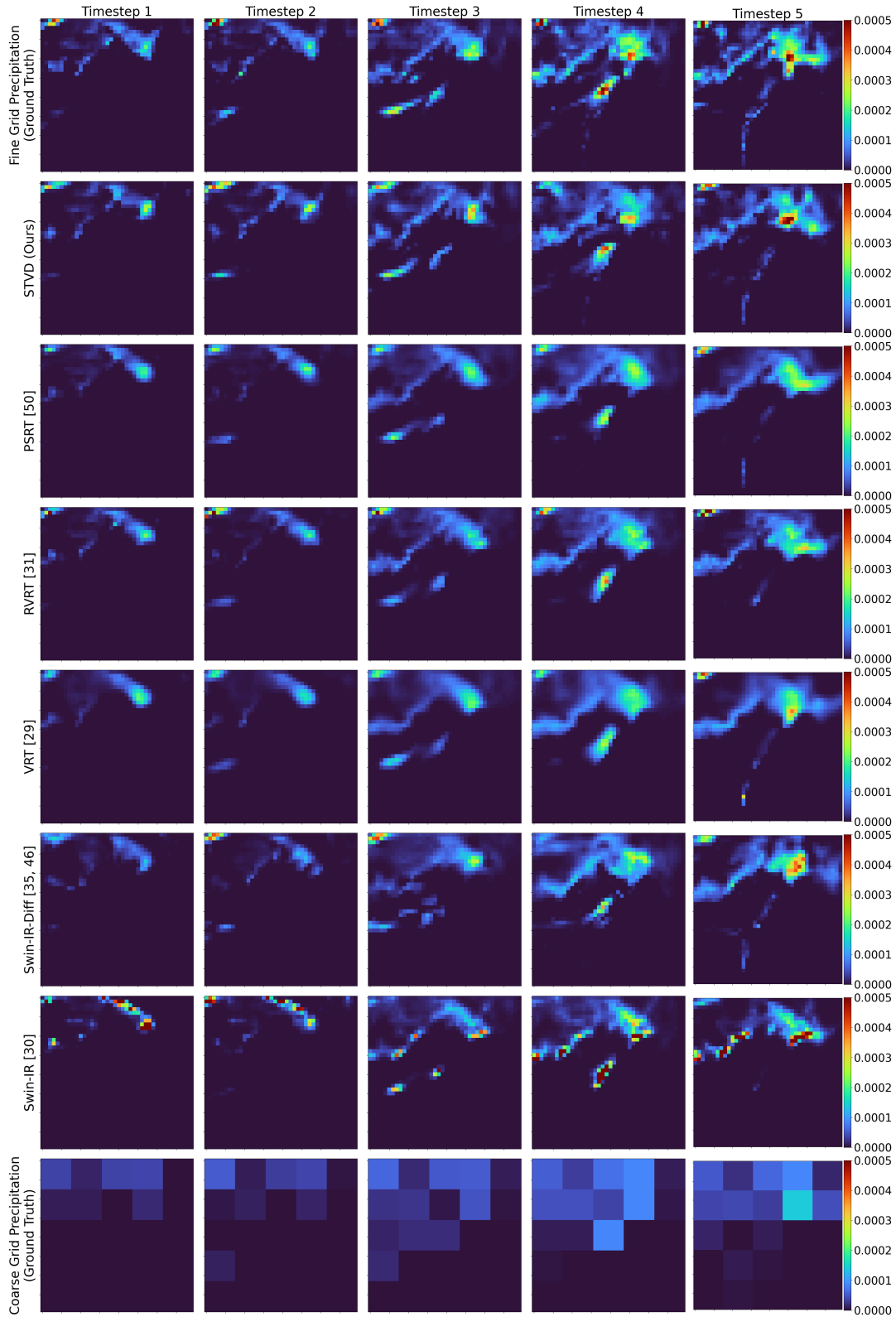


Figure 8: Another qualitative comparison between our proposed model and baselines for a specific precipitation event in the Himalayan mountain range. Fig. 4 (left) plots the regional topography. Similar to Fig. 2, the first row represents the ground truth fine-grid precipitation state sequence, and the last row represents the coarse-grid precipitation that is being downscaled. All other rows correspond to our model and the baseline outputs. The time interval between adjacent frames is 3 hours; the plotted region is 1000×1000 km.

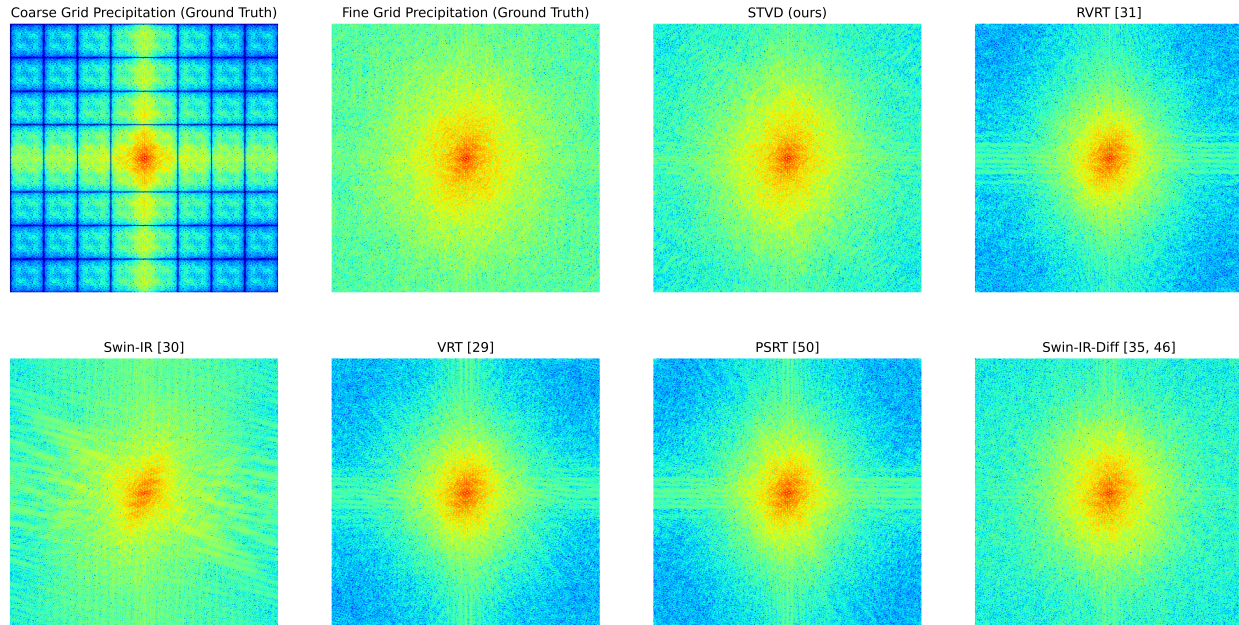


Figure 9: RVRT, VRT, PSRT and Swin-IR-Diff show a spectra which decays too rapidly, i.e. placing too little energy on the high-frequency components. The Swin-IR baseline exhibits artifacts in the spectra. Overall, the spectra of samples from our method most closely match the ground-truth spectra.

A.3.1 Spectra

In Fig. 9, we plot (in log-scale) the squared-magnitude of the complex-valued FFT applied to an image in our evaluation set. Overall, we see that the samples from STVD closely match the ground-truth high resolution spectrum. The baselines RVRT, VSRT and PSRT demonstrate a spectrum which decays too rapidly, placing too little energy in the high-frequency components. Additionally, we see a banding in these spectrums similar to the one observed in ground-truth low resolution spectrum. This indicates that these baselines are overly smooth compared to the ground-truth and follow similar banding patterns of the corresponding low resolution image. For the Swin-IR baseline, we observed outliers of large magnitudes in the generated precipitation maps, which we hypothesize leads to the observed checkerboard pattern seen in the spectrum. Swin-IR-Diff seems to decay the spectra more rapidly than STVD.